

1 **New Insights into the Dynamics that Control the Activity of Ceria-Zirconia Solid**  
2 **Solutions in Thermochemical Water Splitting Cycles**  
3

4 A. Pappacena,<sup>†</sup> M. Rancan,<sup>‡,□</sup> L. Armelao,<sup>‡,□</sup> J. Llorca,<sup>§</sup> W. Ge,<sup>||</sup> B. Ye,<sup>||</sup> A. Lucotti,<sup>‡</sup>  
5 A. Trovarelli,<sup>†</sup> M. Boaro<sup>\*,†</sup>

6 <sup>†</sup> *Dipartimento Politecnico di Ingegneria e Architettura, Università di Udine, Via del Cotonificio*  
7 *108, 33100 Udine, Italy*

8 <sup>‡</sup> *Istituto di Chimica della Materia Condensata e di Tecnologie per l'Energia (ICMATE) –*  
9 *Consiglio Nazionale delle Ricerche (CNR), Via Marzolo 1, 35131 Padova (Italy).*

10 <sup>□</sup> *Dipartimento di Scienze Chimiche, Università di Padova, Via Marzolo 1, 35131 Padova (Italy).*

11 <sup>§</sup> *Institut de Tècniques Energètiques and Barcelona Research Center in Multiscale Science and*  
12 *Engineering, Universitat Politècnica de Catalunya, EEBE, Eduard Maristany 10-14, 08019*  
13 *Barcelona, Spain*

14 <sup>||</sup> *State Key Laboratory of Particle Detection and Electronics, University of Science and Technology*  
15 *of China, Hefei, 230026, P. R. China*

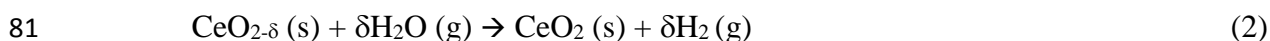
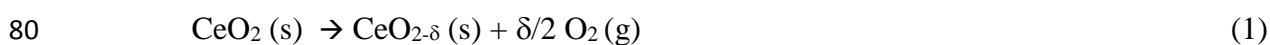
16 <sup>‡</sup> *Dipartimento di Chimica, Materiali ed Ingegneria Chimica "G. Natta", Politecnico di Milano,*  
17 *Piazza Leonardo da Vinci, 32 – 20133 Milano, Italy.*

## ABSTRACT

The reactivity of a ceria-rich  $\text{Ce}_{0.85}\text{Zr}_{0.15}\text{O}_2$  solid solution towards the thermochemical water splitting process (TWS) was studied over repeated  $\text{H}_2/\text{H}_2\text{O}$  redox cycles. The structural and surface modifications after treatment at high temperature under air or  $\text{N}_2$  atmospheres were characterized by High-Resolution Transmission Electron Microscopy (HRTEM), X-ray diffraction (XRD), Raman spectroscopy, X-ray Photoemission Spectroscopy (XPS) and Positron Annihilation Lifetime Spectroscopy (PALS). Samples treated under nitrogen resulted more active due to phase segregation with formation of a zirconyl oxynitride phase in catalytic amount. Insertion of  $\text{N}^{3-}$  into the structure contributes to increase the numbers of oxygen vacancies that preferably arrange in large clusters, and to stabilize  $\text{Ce}^{3+}$  centers on the surface. In comparison, treatment under air resulted in a different arrangement of defects with less  $\text{Ce}^{3+}$  and smaller and more numerous vacancy clusters. This affects charge transfer and H-coupling processes, that play an important role in boosting the rate of  $\text{H}_2$  production. The behavior is found to be only slightly dependent on the starting ceria-zirconia composition and it is related to the development of a similar surface hetero-structure configuration, characterized by the presence of at least a ceria-rich solid solution and a (cerium-doped) zirconyl oxynitride phase, which is supposed to act as a promoter for TWS reaction. The above findings confirm the importance of a multi-phase structure in the design of ceria-zirconia oxides for water splitting reaction and allow a step forward to find an optimal composition. Moreover, the results indicate that doping with nitrogen might be a novel approach for the design of robust, thermally resistant and redox active materials.

## 58 INTRODUCTION

59 The necessity to increase the sustainability of the modern societies requires the development of a  
60 circular economy based on an increasing use of renewable resources for the production of energy  
61 services. Solar energy and water are winner ingredients for improvement of the energy conversion  
62 chain, which would be based on the use of hydrogen or bio-fuels. Among the technologies that exploit  
63 the sunlight to produce ~~energy and~~ fuels, solar thermochemical processes have a good potentiality in  
64 terms of efficiency and there are excellent reviews that summarize the main outcomes in the field.<sup>1-3</sup>  
65 In these processes the solar resource is used directly to drive endothermic chemical reactions such as  
66 the splitting of water (WS) and/or of CO<sub>2</sub> (CDS). Water spontaneously decomposes into elementary  
67 O<sub>2</sub> and H<sub>2</sub> only at temperature higher than 3800 °C.<sup>3</sup> This condition, along with the necessity of  
68 separating O<sub>2</sub> from H<sub>2</sub> makes the direct thermolysis of water impractical. However, the reaction is  
69 possible through multi-steps thermal cycles using specific compounds as promoters. Reducible metal  
70 oxide redox couples such as SnO<sub>2</sub>/SnO, ZnO/Zn, Fe<sub>3</sub>O<sub>4</sub>/FeO, CeO<sub>2</sub>/Ce<sub>2</sub>O<sub>3</sub> have been shown suitable  
71 to split water in two steps: an endothermic step at high temperature (~1200-2000 °C) in which the  
72 oxide is reduced in inert atmosphere and a subsequent exothermic step at lower temperature in which  
73 water oxidizes the metal oxide producing H<sub>2</sub> (~400-1300 °C).<sup>3</sup> The working temperature of each step,  
74 O<sub>2</sub> and H<sub>2</sub> yields, and the fuel purity strongly depend on the type of metal oxide involved. Among  
75 many metal oxides proposed in literature, ceria is one of the most promising candidates.<sup>4</sup> CeO<sub>2</sub> can  
76 be reduced to Ce<sub>2</sub>O<sub>3</sub><sup>5</sup> or to CeO<sub>2-δ</sub> (reaction 1)<sup>4,6</sup> with the aid of solar energy in an inert atmosphere  
77 and at high temperature (1300-1800 °C). Then it can be promptly oxidized by water (reaction 2) at  
78 intermediate temperature (500-800 °C) producing pure H<sub>2</sub> on demand without purification, storage  
79 and transport complications, as conversely encountered in other metal oxide based cycles.



82 Thermodynamic studies of this cycle suggest that solar to fuels efficiency approaching 30% could be  
83 achievable, when a complete heat recovery is accomplished.<sup>7,8</sup> Several experimental and theoretical  
84 studies have identified in the reduction step the main limits of ceria based cycles.<sup>3,9</sup> At a temperature  
85 higher than 1800 °C, which is necessary for a full reduction of CeO<sub>2</sub> to Ce<sub>2</sub>O<sub>3</sub>, CeO<sub>2</sub> starts to  
86 sublime, consequently the yield of cycles has been observed to decrease over the time. At lower  
87 temperatures ceria cannot be fully reduced and H<sub>2</sub> production depends on the degree of reduction  
88 achieved. Therefore, many studies on ceria-based systems have been focused on decreasing the  
89 reduction temperature of the Ce<sup>4+</sup>/Ce<sup>3+</sup> redox couple, while maintaining the high reactivity of reduced  
90 Ce<sup>3+</sup> species towards water.<sup>3,10</sup> The addition of Zr<sup>4+</sup> into the ceria lattice resulted effective in  
91 increasing the thermodynamic driving force of CeO<sub>2</sub> reduction at lower temperatures<sup>11,12</sup>, while  
92 aliovalent dopants have been found less effective.<sup>13,14</sup> New synthesis strategies to control the  
93 morphology and the sintering processes of ceria have also been adopted with success.<sup>15</sup> Most recently  
94 other solutions allowed to obtain a high and stable production of H<sub>2</sub>, such as the addition of rhodium  
95 to ceria lattice as catalyst<sup>16</sup> or the use of a composite of CeO<sub>2</sub> and SnO<sub>2</sub> that under reducing conditions  
96 forms a stoichiometric pyrochlore phase more reactive than the non-stoichiometric CeO<sub>2-δ</sub>.<sup>17</sup>  
97 The effect of zirconium content in the two steps water splitting reaction has been widely studied<sup>13,18-</sup>  
98 <sup>21</sup>; a linear increase of the reduction yields as a function of zirconium content was observed up to a  
99 content of 25 mol%, while at higher contents a stabilization of the released O<sub>2</sub> was recorded. On the  
100 other hand, ceria-zirconia based materials showed a slow kinetics of oxidation.<sup>3,13,21</sup> The oxidation  
101 rate seems to be controlled by intergranular gas-phase diffusion in the material layer. In this case,  
102 improving morphological and textural properties of the mixed oxides via co-doping<sup>22</sup> or by using  
103 different synthesis approaches<sup>13,23</sup> resulted beneficial due to the possibility of tuning the crystalline  
104 size, porosity structure and composition at the nanoscale.<sup>24</sup> Most of the research has been focused on  
105 ceria rich compositions, which were supposed to be structurally stable to the high temperatures  
106 adopted in the reduction step and the attention of scientists was mainly drawn on kinetic and  
107 thermodynamic issues of the cycle. Only a few studies investigated the correlations between water

108 splitting performance and structural/compositional modification undergone during the redox  
109 steps,<sup>23,25</sup> despite it is well known that the redox properties of the materials are markedly affected by  
110 the thermal and redox history.<sup>26</sup> In a recent communication, we showed that also zirconia-rich ceria-  
111 zirconia mixed oxides can be suitable for the WS process.<sup>27</sup> In that study, it appeared clear that phase  
112 segregation and nitridation processes, which were induced by the thermal redox cycles, might play a  
113 major role in determining the high activity. The present study investigates in more detail the WS  
114 behavior of  $\text{Ce}_{0.85}\text{Zr}_{0.15}\text{O}_2$  over more cycles and compares the results with previous outcomes with  
115 the aim to find some commonalities governing the overall behavior of ceria-zirconia in  
116 thermochemical water splitting reactions. Through the use of positron annihilation life time  
117 spectroscopy (PALS) and other complementary techniques we are able to describe for the first time,  
118 not only the characteristics of phases but also the arrangement of defects on the surface of material  
119 when treated at high temperature under air or nitrogen-containing atmospheres. This allows to put  
120 forward a conceivable mechanism that explains the significance of nitridation in the WS activity of  
121 ceria-zirconia oxides.

## 122 **EXPERIMENTAL**

123 **Materials.**  $\text{Ce}_{0.85}\text{Zr}_{0.15}\text{O}_2$  was prepared with a surfactant assisted precipitation method as  
124 reported elsewhere.<sup>28</sup> Briefly, proper amounts of  $\text{Ce}(\text{NO}_3)_3 \cdot 6\text{H}_2\text{O}$  salt (Treibacher Industrie AG) and  
125  $\text{ZrO}(\text{NO}_3)_2$  liquid gel (Treibacher Industrie AG) were dissolved in demineralized water obtaining a  
126 0.2 M solution; concentrated  $\text{H}_2\text{O}_2$  (35% Sigma-Aldrich) was then added according to the molar ratio  
127  $[\text{H}_2\text{O}_2]/[\text{tot metals ions}]$  equal to 3. After 45min of continuous stirring at ambient temperature  
128 concentrated  $\text{NH}_3 \cdot \text{H}_2\text{O}$  (28% Sigma-Aldrich) was added to obtain a pH value of 10.5. Finally, lauric  
129 acid (Sigma-Aldrich), using a molar ratio ( $[\text{tot metal ions}]/[\text{lauric acid}]$ ) equal to 0.25, was directly  
130 added and maintained under continuous stirring for 4h. The precipitate was then filtered and washed  
131 three times with 0.5L of de-mineralized water and the resulting cake was dried at 100 °C overnight.  
132 The dry precipitate was calcined in air at 500 °C for 4h. This method allows to obtain highly

133 homogeneous starting materials, which ensures a reproducible phase segregation. In order to simulate  
134 the aging effect undergone during the strongly endothermic step of TWS cycle, the oxide was treated  
135 at 1300 °C in nitrogen or air for four hours. Other thermal treatment in air were made at 800 °C/4h,  
136 and at 1100 °C. All the samples were cooled down in the atmosphere of treatment and exposed to air  
137 at room temperature before of the reactivity tests.

138

139 **Reactivity tests.** The experimental conditions have been chosen on the basis of previous  
140 studies.<sup>20,23</sup> The activity of  $Ce_{0.85}Zr_{0.15}O_2$ , calcined at 1300 °C/4h either in  $N_2$  (CZ85\_ $N_2$ ) or in air  
141 (CZ85\_ air) was evaluated towards a two steps water splitting thermal cycle using two different setups.  
142 Reduction degree of the material in  $N_2$ /air atmosphere was measured in a thermogravimetric analyser  
143 (Q600-TA Instruments). The thermally aged samples (25mg) were heated at 10°C/min in  $N_2$  flow  
144 (100 ml/min) up to 1300°C. The oxygen released from the oxide was evaluated from the weight loss  
145 observed during 80 minutes of isotherm at 1300 °C. The water splitting (WS) activity was evaluated  
146 in a Micromeritics apparatus using the same method as described by Pappacena et.al.<sup>27</sup> Each sample  
147 (50 mg) was previously reduced to obtain the same reduction degree achieved in the first endothermic  
148 step by using a 5%  $H_2$ /Ar flow and a heating ramp of 10 °C/min up to 700 °C. These conditions have  
149 been established through a thermogravimetry analysis (TGA, Q500-TA Instruments) in 5% $H_2$ /Ar  
150 flow by reducing the sample up to 900 °C. The reduced sample was evacuated in He and oxidized by  
151 20 pulses of water vapor (30% in Ar flow) at 800 °C.  $H_2$  consumption and production were monitored  
152 with a thermal conductivity detector; the total  $H_2$  production was measured by calculating the  $H_2$   
153 outcome from the first twenty water vapor pulses. At the end of the WS reaction the sample was  
154 oxidized with air for 10min to complete the oxidation and cooled down to ambient temperature in He  
155 atmosphere. The cycle was repeated six times. The same experiment was carried out also without  
156 completing the oxidation with air in order to verify whether the oxidation conditions may affect the  
157 reaction of water splitting.

158           **Characterization.** Structural and surface properties of all materials were investigated through  
159 the use of several techniques. X-ray Diffraction analysis (XRD) were performed using a Philips  
160 X'Pert diffractometer operated at 40 kV and 40 mA equipped with a nickel-filtered  $\text{CuK}\alpha$  radiation.  
161 All spectra were collected using a step size of 0.02  $2\theta$  degrees and a counting time of 40s per angular  
162 abscissa in the range of 20–145  $2\theta$  degrees. The Philips X'Pert HighScore software was used for  
163 phases identification. The mean crystalline size was estimated from the full width at the half  
164 maximum (FWHM) of the X-ray diffraction peaks using the Scherrer's equation<sup>29</sup> corrected for the  
165 instrument line broadening. Rietveld refinement of XRD spectra was performed by means of  
166 GSASEXPGUI program.<sup>30,31</sup>

167 Raman spectra have been recorded with a LABRAM HR800 equipped with a solid-state laser (Laser  
168 XTRA, Toptica Photonics) operating at 785 nm and a Peltier cooled CCD detector. The laser radiation  
169 was filtered by an interference filter and was focused on the sample through an Olympus BX41  
170 microscope. A 50X Olympus objective (NA = 0.75) has been used. The Rayleigh radiation was  
171 rejected using Notch filters. In order to ascertain the absence of artifacts the spectra have been  
172 obtained also using excitation radiations, at 512 and 633 nm and two different grids (600 lines/mm;  
173 1800 lines/mm).

174 High resolution transmission electron microscopy (HRTEM) was accomplished with a JEOL J2010F  
175 instrument equipped with a field emission electron source and operated at 200 kV. Samples were  
176 dispersed in alcohol and a drop of the suspension was placed over a grid with holey-carbon film.

177 Specific surface area (SA) and porosity of oxides were measured by nitrogen adsorption/desorption  
178 isotherms at 77 K, following the BET and BJH method respectively<sup>32</sup>, using a Tristar 3000 gas  
179 adsorption analyzer (Micromeritics). The pore size distribution was calculated from the desorption  
180 branch of the isotherm.

181 XPS was used as the main tool to assess the surface chemical composition of the samples before and  
182 after the catalytic process. Analyses were performed on a Perkin-Elmer  $\Phi$  5600-ci spectrometer using

183 non-monochromatized Al K $\alpha$  radiation (1486.6 eV). The spectrometer was calibrated by assuming  
184 the binding energy (BE) of the Au 4f $_{7/2}$  line at 83.9 eV with respect to the Fermi level. The standard  
185 deviation for the BEs values was  $\pm 0.2$  eV. Survey scans were obtained in the 0–1300 eV range (187.8  
186 eV pass energy, 0.4 eV step $^{-1}$ , 0.05 sec step $^{-1}$ ). Detailed scans were recorded for the C1s, O1s, Zr3d  
187 and Ce3d and N1s regions (23.5 eV pass energy, 0.1 eV step $^{-1}$ , 0.1 sec step $^{-1}$ ). The BE shifts were  
188 corrected by assigning to the C1s peak associated with adventitious hydrocarbons a value of 284.8  
189 eV.<sup>33</sup> The analysis involved Shirley-type background subtraction, non-linear least-squares curve  
190 fitting adopting Gaussian-Lorentzian peak shapes, and peak area determination by integration.<sup>34</sup> The  
191 atomic compositions were evaluated from peak areas using sensitivity factors supplied by Perkin-  
192 Elmer, taking into account the geometric configuration of the apparatus.<sup>35</sup> The experimental  
193 uncertainty on the reported atomic composition values does not exceed  $\pm 5\%$ .

194 Positron annihilation lifetime spectroscopy experiments (PALS) were carried out with a fast-slow  
195 coincidence system which has a resolution of 230ps. The scintillation detectors are plastic scintillator  
196 coupled with photomultiplier tubes. A 40 $\mu$ Ci  $^{22}$ Na source of positron was sandwiched between two  
197 pieces of identical samples. For each spectrum about  $2 \times 10^6$  coincidence counts have been recorded  
198 to ensure the repeatability of the measurements. The positron lifetime data were analyzed by the  
199 lifetime9 program with the necessary source corrections.

200

## 201 RESULTS

202 **Reactivity results.** The endothermic step corresponding to the thermal reduction was  
203 evaluated via thermogravimetry by measuring the weight loss of the sample treated at 1300 °C in  
204 N $_2$  or air. O $_2$  released during the thermal treatment was 276  $\mu$ mol/g and 169  $\mu$ mol/g respectively for  
205 the sample aged in N $_2$  and air, which corresponds to a degree of Ce $^{4+}$  reduction of 21 mol% and 13  
206 mol%. Similar results were reported in literature, but generally using higher temperature.<sup>19,20</sup>  
207 Figure 1 shows the results obtained in the exothermic water splitting experiment for both the N $_2$ -  
208 treated oxide and for the sample aged in air. A total of 6 cycles are reported, and the detail for one

209 cycle is shown to the right of the image. N<sub>2</sub>-treated sample is more active, and the H<sub>2</sub> production  
 210 increases significantly up to a stable value obtained with the fourth cycle. A comparison with results  
 211 obtained on Ce<sub>0.15</sub>Zr<sub>0.85</sub>O<sub>2</sub> indicates that regardless of initial composition H<sub>2</sub> yields reach close values  
 212 for the two nitrogen-pretreated compositions after a few cycles.<sup>27</sup> To exclude the role of oxygen in  
 213 the promotion of H<sub>2</sub> production observed from the 2<sup>nd</sup> cycle, the same experiment was repeated  
 214 without oxidizing the samples with air at the end of each cycle, and the results are compared in Figure  
 215 S1.

216 **Characterization results.** Table 1 summarizes the textural and morphological properties of  
 217 Ce<sub>0.85</sub>Zr<sub>0.15</sub>O<sub>2</sub> after thermal treatment in the range of temperatures 500-1300 °C. The material shows  
 218 a good thermal stability up to 800 °C; higher temperatures causes a large drop in surface area with  
 219 values close to 1 m<sup>2</sup>/g after calcination at 1300 °C, regardless of the gas type used in the treatment.  
 220 Correspondingly, an increase of average crystallite size up to 40 nm with loss of porosity is found.  
 221 The structure of the samples was investigated at the nanoscale through XRD, Raman spectroscopy  
 222 and HRTEM.

223  
 224 **Table 1:** Characteristics of Ce<sub>0.85</sub>Zr<sub>0.15</sub>O<sub>2</sub> after the thermal treatments.

Calcination Temperature (°C)	Treatment Atmosphere	Specific Surface Area (m <sup>2</sup> /g) <sup>a</sup>	Pore size (Å)	Crystallite size (Å) <sup>b</sup>
500	Air	94	238	54
800	Air	45	345	99
1100	Air	9	ND	275
1300	Air	1	ND	425
1300	Nitrogen	1	ND	403

225 a: according to BET method; b: determined with Sherrer equation from XRD analysis., ND: not determined

226  
 227 Figure 2 shows the corresponding X-ray diffraction profiles of the samples. After calcination at  
 228 500°C the sample crystallizes in a cubic fluorite structure with a unit cell value of 5.3652(5) Å. This  
 229 value is lower than the one measured for a pure ceria sample, 5.4118(1) Å, and indicative of the  
 230 insertion of Zr<sup>4+</sup> into the ceria lattice. The application of Vegard law<sup>36</sup> allows us to calculate a molar  
 231 doping of zirconium equal to 0.167, that is very close to the nominal composition of the starting

232 material. No large differences exist among the XRD profiles except for the narrowing of the peaks  
233 with the increase of the calcination temperature, indicating sintering of crystallites as a consequence  
234 of the thermal treatments.<sup>37</sup> However, a careful evaluation of the profiles of samples treated at 1300°C  
235 in both air and nitrogen evidences a tiny shift ( $2\theta=0.12\pm 0.4$ ) of the most intense peak (111) of CZ85  
236 to higher angles and a small shoulder at  $2\theta=28.10$  degrees; thus indicating the occurrence of phase  
237 segregation accompanied by small changes in the composition of the cubic CZ85 phase. The small  
238 peak at  $2\theta=28.10$  is attributable to the presence of a monoclinic zirconia-rich phase, ( $\text{Ce}_{0.05}\text{Zr}_{0.95}\text{O}_2$ ,  
239 PDF 88-2392). The XRD profile of the samples sintered in air shows also a small peak at  $2\theta=29.83$   
240 which is probably related to a tetragonal zirconia-rich phase ( $\text{Ce}_{0.18}\text{Zr}_{0.82}\text{O}_2$ , PDF 80-0785) or to  
241 tetragonal  $\text{ZrO}_2$  (JCPDS 01-080-0785). Such type of segregation is consistent with what is reported  
242 in literature for similar compositions.<sup>38</sup>

243 Figure 3 shows the Raman spectra of samples treated at 1300 °C before and after WS cycles. Figure  
244 S2 shows also the spectra collected using excitation lines at 512 and 633 nm. Spectra in the region  
245  $180\text{-}800\text{ cm}^{-1}$  are characterized by an intense signal at ca.  $476\text{ cm}^{-1}$  corresponding to the fundamental  
246 vibration mode  $\text{F}_{2g}$  of the fluorite structure and satellite bands at 300 and  $602\text{ cm}^{-1}$ , consistent with a  
247 distortion of the cubic structure and the presence of a tetragonal  $t''$  phase.<sup>39</sup> The minority phases are  
248 not detectable and the spectra of the samples before and after WS cycles are almost identical. Above  
249  $1000\text{ cm}^{-1}$  all the spectra show complex bands which are generally attributable to electronic f-f  
250 transitions of  $\text{Ln}^{3+}$  ions present as impurities in the materials.<sup>38</sup> Alternatively, these bands have been  
251 also associated to the presence of  $\text{Ce}^{3+}$  ions.<sup>39,41,42</sup> It is interesting to note that the intensity of these  
252 bands, which is generally related to the asymmetry of the sites, increases after the cycles.

253 Figure 4A shows a HRTEM image of the sample treated in nitrogen at high temperature. The  
254 crystallite labeled “a” corresponds to a single cubic CZ particle oriented along the [110]  
255 crystallographic direction. Spots at  $3.0\text{ \AA}$  correspond to the cubic (111) planes. In contrast, the  
256 crystallite labeled “b” shows a FT pattern exhibiting spots aligned at  $2.5$  and  $5.1\text{ \AA}$  as well as spots at

257 2.9 Å. The spots aligned at 2.5 and 5.1 Å are ascribed to the (400) and (200) crystallographic planes  
258 of Zr<sub>2</sub>ON<sub>2</sub>, respectively, whereas those at 2.9 Å correspond to the (222) planes of Zr<sub>2</sub>ON<sub>2</sub>.  
259 These results are in good agreement with those reported in literature<sup>42</sup>, except for tiny differences  
260 which could be explained with the insertion of cerium in the structure. This hypothesis is reasonable  
261 considering that Ce<sup>3+</sup> (103 pm) has an effective ionic radius similar to that of La<sup>3+</sup>, and that the  
262 formation of LaZrO<sub>2</sub>N has been demonstrated.<sup>44</sup> The HRTEM analysis of sample treated in air (Figure  
263 4B) does not evidence the presence of the oxynitride phase. FT image with spots at 3.0 Å corresponds  
264 to the (111) planes of cubic CZ, which is the dominant phase. The effects of WS cycles at the  
265 nanoscale are shown in Figure 4C. The TEM image (left) evidences a sample constituted by  
266 crystallites measuring more than 100 nm in a compact arrangement, suggesting that the sample  
267 sintered during the cycles. Triple junctions are easily recognized, which usually appear upon high  
268 temperature calcination treatments. The figure at the right corresponds to a representative HRTEM  
269 image of the sample. In this case, only lattice fringes corresponding to the CZ oxide are recognized.  
270 In the figure, several lattice fringes are indicated and correspond to the (111), (220) and (222)  
271 crystallographic planes of cubic CZ at 3.0, 1.8 and 1.5 Å, respectively.  
272 The composition and defects structure of samples before and after WS cycles are investigated through  
273 XPS and PALS techniques. Figures 5A and B show the XPS spectra and the corresponding fitting  
274 components of Ce3d and O1s regions for the samples treated at 1300 °C in nitrogen. Similar features  
275 were observed for the air-treated sample and for the samples after six WS cycles (see Figure S3 and  
276 S4). Figures 5C and D show the N1s region of the sample treated in nitrogen before and after WS  
277 cycles.  
278 In Figure 5A, U and V refer to cerium 3d<sub>3/2</sub> and 3d<sub>5/2</sub> spin-orbit components, respectively. U, U'', U''',  
279 V, V'', and V''' refer to the final states of Ce<sup>4+</sup>, while U°, U' and V°, V' refer to those of Ce<sup>3+</sup> [25].  
280 The fitted peak areas were used to estimate the relative amount of Ce<sup>3+</sup> and Ce<sup>4+</sup> (see Table 2). The  
281 O1s region is suitably fitted with two components (Figure 5B). The main component (peak 1) at about  
282 529.5 eV is associated with the cerium–zirconium oxide matrix, while the component centered at

283 531.5 eV (peak 2) can be ascribable mainly to surface hydroxyl groups.<sup>44</sup> The signal N1s at 399.9 eV  
284 (Figure 5C) confirmed the insertion of nitrogen into the surface of the CZ85\_N<sub>2</sub> and the formation of  
285 a zirconyl oxynitride phase<sup>27,46,47</sup> In addition, the evidence of the same nitrogen peak on the CZ85\_N<sub>2</sub>  
286 surface after WS cycles (CZ85\_N<sub>2</sub>\_ws, Figures 5D) indicates that the oxynitride phase is stable under  
287 WS conditions. No signal corresponding to insertion of nitrogen is observed for samples treated under  
288 air.

289 Table 2 summarizes the surface chemical composition (atomic %) of the samples, determined from  
290 the analysis of Ce3d and Zr3d XPS peaks.

291 Sample calcined at 500 and 1100 °C show a surface composition consistent with the nominal  
292 stoichiometry of the Ce<sub>0.85</sub>Zr<sub>0.15</sub>O<sub>2</sub> solid solution revealing that the starting material was  
293 homogeneous and thermally stable up to 1100 °C. After treatment at 1300 °C the value of Zr/Ce ratio  
294 increase to 0.26 in agreement with the phase segregation observed by XRD and indicating that  
295 zirconia-rich compositions are mainly located on the outer part of the crystallite. The presence of Ce<sup>3+</sup>  
296 in the starting material (500 °C) is due to the nanometric nature of the powder and to the presence of  
297 extrinsic defects induced by the zirconium doping.<sup>38</sup> Besides, a small quantity of Ce<sup>3+</sup> could be  
298 generated by the reduction of Ce<sup>4+</sup> under the X-ray irradiation during XPS analysis.<sup>48</sup> The amount of  
299 Ce<sup>3+</sup> increased after calcination at 1100 and 1300 °C as expected from the state diagrams of CeO<sub>2</sub> in  
300 air and N<sub>2</sub> conditions, for which CeO<sub>2</sub> starts reducing above 1000 °C.<sup>4,6</sup> After water splitting cycles  
301 the concentration of Ce<sup>3+</sup> remained the same for the sample treated in nitrogen, while it slightly  
302 decreased in the case of the sample pretreated in air. For the N<sub>2</sub> treated sample the extent of surface  
303 nitridation, was determined from the N/Ce atomic ratio which resulted similar before and after the  
304 WS reaction, with a value of ca. 0.03. However, due to the very low intensity of the N1s peak, this is  
305 only a rough estimate.

306

307 Table 2. Results of XPS analysis

Sample	Ce <sup>b</sup> [Ce <sup>3+</sup> , Ce <sup>4+</sup> ] <sup>c</sup>	Zr <sup>b</sup>	Zr/Ce	Ce <sup>3+</sup> /Ce <sup>4+</sup>
CZ85-500 <sup>a</sup>	84.2 [14.3, 69.9]	15.8	0.19	0.20
CZ85-1100 <sup>a</sup>	85.4 [22.2, 63.2]	14.6	0.17	0.35
CZ85_air	79.0 [22.1, 56.9]	21.0	0.26	0.39
CZ85_N2	79.1 [24.5, 54.6]	20.9	0.26	0.45
CZ85_air_WS	79.8 [18.4, 61.4]	20.2	0.26	0.30
CZ85_N2_WS	79.1 [24.5, 54.6]	20.9	0.26	0.45

308 a - the number indicates the temperature of calcination in air; b-the uncertainty on the quantitative values does not exceed  
309  $\pm 5\%$ , c - values obtained from fitting of the Ce3d region.  
310

311 Details into the organization of surface defects were obtained via positron annihilation lifetime  
312 spectroscopy (PALS). Figure S5 shows the PALS spectra for some representative sample. All spectra  
313 were fitting to three lifetime components ( $\tau_1$ ,  $\tau_2$ ,  $\tau_3$ ) and the corresponding values along with their  
314 relative intensity ( $I_1$ ,  $I_2$ ,  $I_3$ ) are summarized in Table 3. As far as we know, this is the first time that  
315 PALS technique is applied to the characterization of CZ85 mixed oxides, therefore we used a CZ85  
316 sample calcined at 1100 °C as a reference material for an interpretation of the data. Since the  
317 temperature used for treatment is not enough high to cause phase segregation and thermal reduction,  
318 such a sample is representative of a homogeneous highly sintered composition.

319 The longest component  $\tau_3$  is attributed to the annihilation of orthopositronium atoms formed in the  
320 large voids present in the material.<sup>49</sup> It hardly helps in giving some useful information of defects in  
321 the samples because the formation of the orthopositronium atoms are not related to the positron  
322 trapping at defects, so it will be neglected in the following discussion. The component  $\tau_1$  is generally  
323 attributed to the free annihilation of positrons in defect-free crystal. However, for disordered systems  
324 it may also be associated to small defects (like mono vacancies) and shallow positrons traps (like  
325 oxygen vacancies), which can decrease the average electron density and elongation of  $\tau_1$ .<sup>50,51</sup>

**Table 3:** Peak-fitting results of PALS spectra, Spectra fitted with the Lifetime9 software.

sample	$\tau_1$ (ps)	$\tau_2$ (ps)	$\tau_3$ (ns)	$I_1$ (%)	$I_2$ (%)	$I_3$ (%)
<b>CZ85_air</b>	170.8	310.0	1.09	78.9	20.8	0.35
<b>CZ85_N<sub>2</sub></b>	175.2	358.0	1.02	72.2	26.6	1.20
<b>CZ85_N<sub>2</sub>_ws</b>	173.7	351	1.83	83.9	15.5	0.53
<b>CZ85_air_ws</b>	164.4	291	1.4	74.6	25.0	0.44
<b>CZ85-1100</b>	179.1	359	0.95	47.2	51.9	0.88

326

327 In many studies on ceria based oxides in form of nano-powders, this first component  $\tau_1$  has been  
328 related to neutral oxygen mono-vacancies associated to  $Ce^{3+}$  ( $Ce'_{ce}V_{\bullet\bullet}O_{ce}$ ) according to Kröger  
329 and Vink's defect notation).<sup>52</sup> From Table 3 we can see the  $\tau_1$  values are about ~175 ps, which are far  
330 lower than that reported in literature, indicating that the small vacancies have higher electron density  
331 in our samples. Such a difference might be due to the fact that, in our case, the material has a larger  
332 crystal size owing to its sintering at high temperature.<sup>51</sup> The component  $\tau_2$  is much larger than the  
333 component  $\tau_1$ , and it arises from positrons trapped by larger size defects. These type of defects mainly  
334 locate on the surface or subsurface, thus  $\tau_2$  should give useful information on the surface defects of  
335 samples.<sup>52,54</sup>

336 It is worth noting that the values of  $\tau_1$  and  $\tau_2$  for the reference sample CZ85-1100 are very similar to  
337 the respective life times for the sample treated in nitrogen before the test (CZ85\_N<sub>2</sub>). Conversely, the  
338 related intensity  $I_1$  and  $I_2$  are different, the thermal treatment in nitrogen leads to a decrease of the  
339 number of large size clusters on the surface with respect to the reference. The sample treated in air  
340 (CZ85\_air) shows a lower value of  $\tau_2$ . Taking into account that the electron density is lower in the  
341 large size clusters rather than in the small defects, and consequently the positron lifetime increases in  
342 the larger size defects, it is inferred that in the air-treated sample the clusters of defects are smaller  
343 than in the N<sub>2</sub>-treated sample or in the reference. Moreover, by comparing the ratio  $I_1/I_2$  of the two

344 samples heated at 1300 °C, it is clear that the material treated in nitrogen have a higher clusters density  
345 than that treated in air.

346 After WS cycles, both the samples treated in nitrogen and that treated in air showed lower values of  
347  $\tau_1$  and  $\tau_2$ . The entity of the decrease is more significant for the sample treated in air (CZ85\_air\_ws)  
348 rather than for the sample treated in nitrogen (CZ85\_N<sub>2</sub>\_ws). Opposite trends have been observed for  
349 the value of  $I_2$  in the two samples. After cycles the value of  $I_2$  diminished of the 37% for the  
350 CZ85\_N<sub>2</sub>\_ws, while increased 20% for the CZ85\_air\_ws. That implies respectively a less or higher  
351 number of defects clusters in the two samples after reaction.

## 352 **DISCUSSION**

353 The results indicate that thermal treatment either in N<sub>2</sub> or air at high temperature of Ce<sub>0.85</sub>Zr<sub>0.15</sub>O<sub>2</sub>  
354 induces subtle structural changes promoting phase segregation. The material treated under nitrogen  
355 shows the formation of a zirconia based oxy-nitride phase located at the outer part of the grains that  
356 is beneficial for the water splitting reaction. The active phase is composed by this oxynitride phase  
357 which is present in catalytic amount and by a pseudo-cubic oxide rich in ceria (Ce<sub>x</sub>Zr<sub>1-x</sub>O<sub>2- $\delta$</sub> , 0.7 $\leq$ x $\leq$   
358 0.9) as a major phase. This study uses XPS and PALS to obtain more details into the defects  
359 organization of these heterogeneous structures to see how the structure and quantity of oxygen  
360 vacancies can help in developing more stable and robust WS catalysts.

361 In agreement with previous observations, our findings confirmed that the main surface defects in  
362 ceria–zirconia oxide are polarons, which are related to Ce<sup>3+</sup> centers, and oxygen vacancies.<sup>55</sup> XPS  
363 analysis accounts for the number of Ce<sup>3+</sup> (Table 2) while PALS technique gives information on the  
364 organization of oxygen vacancies (Table 3). The material treated in nitrogen shows a higher  
365 concentration of Ce<sup>3+</sup> and larger oxygen vacancy clusters at its surface in comparison to the sample  
366 treated in air. Moreover, the configuration of these defects remains almost the same after redox cycles  
367 (the same amount of Ce<sup>3+</sup> and the same dimensions of cluster, even if clusters number decreased).  
368 Conversely, the sample treated under air shows a new arrangement of defects with the presence of

369 smaller and more numerous vacancy clusters and a decreased amount of  $\text{Ce}^{3+}$  at the surface. Since  
370 the thermal treatments in nitrogen or air caused similar structural and compositional changes in the  
371 oxide material, the different configuration of vacancies in air and  $\text{N}_2$  treated materials has to be related  
372 with the nitridation process and the initial reduction degree of the two materials. Assuming that charge  
373 neutrality has to be preserved, the substitution of  $\text{O}^{2-}$  anions with  $\text{N}^{3-}$  must be balanced by the  
374 introduction of oxygen vacancies.<sup>56</sup> The addition of these extra vacancies along with the necessary  
375 vacancies to balance  $\text{Ce}^{3+}$  charges, (more numerous in the sample treated in nitrogen because more  
376 reduced) may justify the formation of larger vacancy clusters in the sample treated in nitrogen.  
377 Defects configurations after testing are related to samples oxidized with water, and the differences  
378 observed for the two materials suggest that water splitting proceeded through different pathways. We  
379 can put forward some hypotheses on basis of recent theoretical and experimental studies regarding  
380 the stability and behavior of reduced  $\text{CeO}_2(111)$  surface when interacting with water.<sup>57</sup> It is reported  
381 that large surface vacancy clusters are formed and stabilized via a “hydroxyl-vacancies model”.<sup>58</sup> The  
382 coexistence of hydroxyl groups and vacancies at the subsurface of  $\text{CeO}_{2-x}(111)$  favors the stabilization  
383 of vacancy dimers or trimers at the surface. Large clusters at the surface in turns favor the mobility  
384 of H in the bulk and a higher concentration of  $\text{Ce}^{3+}$  at the surface.<sup>59</sup> The formation and presence of  
385 subsurface hydroxyl groups favor the H transfer between neighboring top-surface O and subsurface  
386 O rather than the direct surface diffusion of H among top surface O, because of the lower energy  
387 barrier of the mechanism.<sup>58</sup> The high concentration of  $\text{Ce}^{3+}$  at the surface, close to vacancy clusters  
388 leads to a more significant charge modification of the neighboring surface O pushing more covalent  
389 electrons towards O. This would contribute to weaken the H-O bond and, consequently, benefit the  
390 process of H coupling, which requires O-H bond breaking, to form  $\text{H}_2$ .

391 The water splitting process involves surface reactions (i.e. adsorption/dissociation of water,  
392 ion/electron transfer on the surface and association of H atoms and  $\text{H}_2$  desorption), and incorporation  
393 of ions into the bulk. Recently it has been demonstrated that in ceria-zirconia based materials the  
394 surface oxygen-ions transfer, mediated by bulk oxygen vacancies is fast and that the rate determining

395 step of reaction is related to the reduction of hydroxyl groups, and to the release of H<sub>2</sub>, rather than  
396 due to the incorporation of ions into the bulk.<sup>60,55</sup>

397 Our results agree with the idea illustrated in Figure 6. The oxynitride phase contributes to create and  
398 stabilize large vacancy oxygen clusters<sup>61</sup> that at the first cycle can be easily hydroxylated (Figure 6  
399 A-C). The co-existence of these large clusters and hydroxyl groups helps maintaining reduced surface  
400 through a rapid replacement of vacancies from the bulk and an incorporation of hydroxyl groups into  
401 the subsurface layers of the oxide (Figure 6 D). This configuration contributes to boost the rate  
402 determining step of water splitting to produce H<sub>2</sub>, thus explaining the higher reactivity of the material  
403 treated in N<sub>2</sub> from the second cycle. In this view, the material treated under air lacks of suitable centers  
404 to induce hydroxylation of subsurface and the reaction will be limited at the surface with a less  
405 effective rearrangement of defects over cycles.

406 This study allows also to clarify and explain the behavior of Zr-rich compositions like Ce<sub>0.15</sub>Zr<sub>0.85</sub>O<sub>2</sub>.<sup>27</sup>  
407 Despite this latter composition is less thermally stable and shows a more significant surface  
408 segregation under nitrogen flow, the final composition at the outer part of the particles is similar to  
409 that observed for Ce<sub>0.85</sub>Zr<sub>0.15</sub>O<sub>2</sub>. Figure 7 summarizes the main steps of the transformation for both  
410 compositions trying to elucidate the reasons why ceria-rich and zirconia-rich materials show similar  
411 water splitting reactivity after thermal treatment in nitrogen and redox activation. It is worth noting  
412 that after thermal treatment we end up with a surface phase arrangement which is characterized by  
413 the co-presence of Ce<sub>x</sub>Zr<sub>1-x</sub>O<sub>2-δ</sub>, 0.7 ≤ x ≤ 0.9 and Zr<sub>2</sub>ON<sub>2</sub>, which is formed from the nitridation of  
414 segregated zirconia and is stable under redox cycles. The possibility that under our conditions the  
415 oxynitride phase might be doped with cerium cannot be excluded, and further investigations are  
416 requested to better address the nitridation mechanism and the stability of such phases.

417

418 **CONCLUSIONS**

419 This study investigates the structural changes occurring on  $Ce_{0.85}Zr_{0.15}O_2$  during thermochemical  
420 water splitting cycles. It is found that thermal aging in nitrogen atmosphere modifies the surface  
421 structure and composition of the materials by promoting the segregation of a ceria-zirconia solid  
422 solution rich in ceria along with a zirconia-oxynitride phase, a fate that is similar to that found over  
423 zirconia-rich compositions. Positron Annihilation Lifetime Spectroscopy measurements have shown  
424 that the oxynitride phase contributes to form large surface vacancy clusters with an appropriate defect  
425 configuration which promotes charge transfer and H coupling, thus playing a pivotal role in boosting  
426 the production of  $H_2$ . Modification in the size distribution and number of structural defects can  
427 explain the different behavior when the material is treated under air atmosphere.

428 All these findings suggest new approaches for the development and design of ceria based materials  
429 for the two-step water splitting reaction and highlight the importance of engineering the surface defect  
430 structure/configuration of the material to obtain an efficient catalyst. In this regard, the role and the  
431 impact of nitridation process need to be further investigated.

432

## 433 **ASSOCIATED CONTENT**

### 434 **Supporting Information**

435 Reactivity test, Raman spectra, XPS, HRTEM, PALS spectra

## 436 **AUTHOR INFORMATION**

### 437 **Corresponding Author**

438 \* E-mail: [marta.boaro@uniud.it](mailto:marta.boaro@uniud.it). Tel.:(+39)0432-558825. Fax (+39)0432-558803

439

## 440 **REFERENCES**

441 (1) Miller, J.E.; McDaniel, A.H.; Allendorf, M.D. Considerations in the Design of Materials for Solar-  
442 Driven Fuel Production Using Metal-Oxide Thermochemical Cycles. *Adv. Energy Mater.* **2014**, *4*, 1-  
443 19.

444 (2) Agrafiotis, C.; Roeb M.; Sattler, C.A Review on Solar Thermal Syngas Production via Redox  
445 Pair-Based Water/Carbon Dioxide Splitting Thermochemical Cycles. *Ren. Sust. Energy* **2015**, *42*,  
446 254-285.

- 447 (3) Scheffe, J.R.; Steinfeld, A. Oxygen Exchange Materials for Solar Thermochemical Splitting of  
448 H<sub>2</sub>O and CO<sub>2</sub>: a review. *Mat. Today* **2014**, *17*, 341-348.
- 449 (4) William, C.C.; Haile, M.S. Thermochemical Study of Ceria: Exploiting and Old Material for New  
450 Modes of Energy Conversion and CO<sub>2</sub> Mitigation. *Phil. Trans. R. Soc. A* **2010**, *368*, 3269-3294.
- 451 (5) Abanades, S.; Flamant, G. Thermochemical Hydrogen Production from a Two-Step Solar-Driven  
452 Water-Splitting Cycle Based on Cerium Oxides. *SolarEnergy* **2006**, *80*, 1611-1623.
- 453 (6) Chueh, W.C.; Falter, C.; Abbott, M.; Scipio, D.; Furler, P.; Haile, S.M.; Steinfeld, A. High-Flux  
454 Solar-Driven Thermochemical Dissociation of CO<sub>2</sub> and H<sub>2</sub>O Using non-Stoichiometric Ceria.  
455 *Science* **2010**, *330*, 1797-1801.
- 456 (7) Lapp, J.; Davidson, J.H.; Lipiński, W. Efficiency of two-step Solar Thermochemical Non-  
457 Stoichiometric Redox Cycles with Heat Recovery. *Energy* **2012**, *37*, 591-600.
- 458 (8) Siegel, N.P.; Miller, J.E.; Ermanoski, I.; Diver, R.B.; Stechel, E.B. Factors Affecting the  
459 Efficiency of Solar Driven Metal Oxide Thermochemical Cycles. *Ind. Eng. Chem. Res.* **2013**, *52*,  
460 3276-3286.
- 461 (9) Bufin, B.; Call, F.; Lange, M.; Lübben, O.; Sattler, C.; Pitz-Paal, R.; Shvets I.V. Thermodynamics  
462 of CeO<sub>2</sub> Thermochemical Fuel Production. *Energy Fuels* **2015**, *29*, 1001-1009.
- 463 (10) Scheffe, J.R.; Steinfeld, A. Thermodynamic Analysis of Cerium-Based Oxides for Solar  
464 Thermochemical Fuel Production. *Fuels* **2012**, *26*, 1928–1936.
- 465 (11) Kim, T.; Vohs, J.M.; Gorte, R.J. Thermodynamic Investigation of the Redox Properties of  
466 Ceria-Zirconia Solid solutions. *Ind. Eng. Chem. Res.* **2006**, *45*, 5561-5565.  
467
- 468 (12) Hao, Y.; Yang, C.-K.; Haile, S.M. Ceria-Zirconia Solid Solutions (Ce<sub>1-x</sub>Zr<sub>x</sub>O<sub>2-δ</sub>, x ≤ 0.2) for  
469 Solar Thermochemical Water Splitting: A Thermodynamic Study. *Chem. Mater.* **2014**, *26*,  
470 6073–6082.
- 471
- 472 (13) Le Gal, A.; Abanades, S.; Bion, N.; Le Mercier, T.; Harlé, V. Reactivity of doped Ceria-Based  
473 Mixed Oxides for solar Thermochemical Hydrogen generation via Two Step Water Splitting Cycles.  
474 *Energy Fuel* **2013**, *27*, 6068-6078.
- 475 (14) Le Gal, A.; Abanades, S. Dopants Incorporation in Ceria for Enhanced Water Splitting: Activity  
476 During Solar Thermochemical Hydrogen Generation. *J. Phys. Chem. C* **2012**, *116*, 13516-13523.
- 477 (15) Rudisill, S.G.; Venstrom, L.J.; Petkovich, N.D.; Quan, T.; Hein, N.; Boman, D.B.; Davidson,  
478 A.; Stein, J.H. Enhanced Oxidation Kinetics in Thermochemical Cycling of CeO<sub>2</sub> through template  
479 porosity. *J. Phys. Chem C* **2013**, *117*, 1692-1700.
- 480 (16) Lin F.J.; Rothensteiner, M.; Alxneit I.; van Bokhoven, J.A.; Wokaun, A. First demonstration of  
481 direct hydrocarbon fuel production from water and carbon dioxide by solar-driven thermochemical  
482 cycles using rhodium-ceria. *Energy Environ Sci.* **2016**, *9*, 2400-2409.
- 483 (17) Ruan, C.; Tan, Y.; Li, L.; Wang, J.; Liu, X.; Wang, X. A novel CeO<sub>2-x</sub>SnO<sub>2</sub>/Ce<sub>2</sub>Sn<sub>2</sub>O<sub>7</sub> Pyrochlore  
484 Cycles for Enhanced Solar Thermochemical Water Splitting. *AIChE J.*, **2017**. *63*, 3450-3463.

- 485 (18) Kaneko, H.; Taku, S.; Tamaura, T. Reduction Reactivity of CeO<sub>2</sub>-ZrO<sub>2</sub> Oxide Under High O<sub>2</sub>  
486 Partial Pressure in Two-Step Water Splitting Process. *Solar Energy* **2011**, *85*, 2321-2330.
- 487 (19) Le Gal, A.; Abanades, S.; Flamant, G. CO<sub>2</sub> and H<sub>2</sub>O Splitting for Thermochemical Production  
488 of Solar Fuels using Non-Stoichiometric Ceria and Ceria/Zirconia Solid Solutions. *Energy Fuels*  
489 **2011**, *25*, 4836-4845.
- 490 (20) Le Gal, A.; Abanades, S. Catalytic Investigation of Ceria-Zirconia Solid Solutions for Solar  
491 Hydrogen Production. *Int. J. Hydrogen Energy* **2011**, *36*, 4739-4748.
- 492 (21) Bulfin, B.; Lange, M.; de Oliveira, L.; Roeb, M.; Sattler, C. Solar Thermochemical Hydrogen  
493 Production Using Ceria Zirconia Solid Solutions: Efficiency analysis. *Int. J. Hydrogen Energy* **2016**,  
494 *41*, 19320-19328.
- 495 (22) Dasari, H.P.; Ahn, K.; Park, S.-Y.; Ji, H.-I.; Yoon, K.J.; Kim, B.-K.; Je, H.-J.; Lee, H.-W.; Lee,  
496 J.-H. Hydrogen Production from Water-Splitting Reaction Based on RE-Doped Ceria-Zirconia  
497 Solid-Solutions. *Int. J. Hydrogen Energy* **2011**, *38*, 6097-6103.  
498
- 499 (23) Petkovich, N.D.; Rudisill, S.G.; Venstrom, L.J.; Boman, D.B.; Davidson J.H.; Stein, A. Control  
500 of Heterogeneity in Nanostructured Ce<sub>1-x</sub>Zr<sub>x</sub>O<sub>2</sub> Binary Oxides for Enhanced Thermal Stability and  
501 Water Splitting Activity. *J. Phys. Chem. C*, **2011**, *115*, 21022-21033.
- 502 (24) Wu, K.; Sun, L.-D.; Yan, C.H. Recent Progress in Well-Controlled Synthesis of Ceria-Based  
503 Nanocatalysts towards Enhanced Catalytic Performance. *Adv. Energy Mater.* **2016**, *6*, 1-46.
- 504 (25) Pappacena, A.; Boaro, M.; Šolcová, O.; Trovarelli, A. *Trans Tech Publications*, Ceria Based  
505 Materials with Enhanced OSC Properties for H<sub>2</sub> Production by Water Splitting Reaction Advances in  
506 Science and Technology. **2014**, *93*, 76-81
- 507 (26) Boaro, M.; Desinan, S.; Abate, C.; Ferluga, M.; de Leitenburg, C.; Trovarelli, A. Study on Redox,  
508 Structural and Electrical Properties of Ce<sub>x</sub>Zr<sub>1-x</sub>O<sub>2</sub> for Applications in SOFC Anodes. *J. Electrochem.*  
509 *Soc.* **2011**, *158*, P22-29.
- 510 (27) Pappacena, A.; Boaro, M.; Armelao, L.; Llorca, J.; Trovarelli, A. Water Splitting Reaction on  
511 Ce<sub>0.15</sub>Zr<sub>0.85</sub>O<sub>2</sub> Driven by Surface Heterogeneity. *Catal. Sci. Technol.* **2016**, *6*, 399-403.
- 512 (28) Pappacena, A.; Scherzanz, K.; Sagar, A.; Aneggi, E.; Trovarelli, A. Development of a Modified  
513 Co-Precipitation Route for Thermally Resistant, High Surface Area Ceria-Zirconia Based Solid  
514 Solutions *Stud. Surf. Sci. Catal.* **2010**, *175*, 835-838.
- 515 (29) Warren, B.E.; *X-ray Diffraction*; Dover Publications INC: New York, 1990.
- 516 (30) Toby, B. H. J. *Appl. Crystallogr.* **2001**, *34*, 210-213.
- 517 (31) Larson, A. C.; Dreele, R. B. V. *General Structure Analysis System "GSAS"*; Los Alamos  
518 National Laboratory: Los Alamos, NM, 2000.
- 519 (32) Lowell, S.; Shields, J.E.; Thomas, M.A.; Thommes, M. *Characterization of Porous Solids and*  
520 *Powders: Surface Area, Pore Size and Density*; Kluwer Academic Publisher, Springer: Dordrecht,  
521 2006.
- 522 (33) Briggs D.; Seah, M. *In Practical Surface Analysis*; Ed. Wiley: Chichester, 1990.

- 523 (34) Shirley, D.A. High-Resolution X-Ray Photoemission Spectrum of the Valence Bands of Gold.  
524 *Phys. Rev. B: Condens. Matter.* **1972**, *5*, 4709-4714.
- 525 (35) Moulder, J.F.; Stickle, W.F.; Sobol, P.E.; Bomben, K.D. *Handbook of X-ray Photoelectron*  
526 *Spectroscopy, Physical Electronics*, J. Chastain (Ed.): Eden Prairie, MN, 1992.
- 527 (36) Hong, S.J.; Virkar, A.V. Lattice Parameters and Densities of Rare-Earth Oxide Doped Ceria  
528 Electrolytes. *J. Am. Ceram. Soc.* **1995**, *78*, 433-439.
- 529 (37) Zhang, F.; Chen, C.-H.; Hanson, J.C.; Robinson, R.D.; Herman, I.P.; Chan, S.-W. Phases in  
530 Ceria-Zirconia Binary Oxide (1-x)CeO<sub>2</sub>-xZrO<sub>2</sub> Nanoparticles: the Effect of Particle Size. *J. Am.*  
531 *Ceram. Soc.* **2006**, *89*, 1028-1036.
- 532 (38) Prusty, D.; Pathaka, A.; Mukherjee, M.; Mukherjee, B.; Chowdhury, A. TEM and XPS  
533 Studies on the Faceted Nanocrystals of Ce<sub>0.8</sub>Zr<sub>0.2</sub>O<sub>2</sub>. *Mater. Charact.* **2015**, *100*, 31-35.
- 534 (39) Kaspar, J.; Fornasiero, P.; Balducci, G.; Di Monte, R.; Hickey, N.; Sergio, V. Effect of ZrO<sub>2</sub>  
535 Content on Textural and Structural Properties of CeO<sub>2</sub>/ZrO<sub>2</sub> Solid Solutions Made by Citrate  
536 Complexation Route. *Inorg. Chim. Acta* **2003**, *349*, 217-226.
- 537 (40) Fornasiero, P.; Speghini, A.; Di Monte, R.; Bettinelli, M.; Kašpar, J.; Bigotto, A.; Sergio, V.;  
538 Graziani, M. Laser-Excited Luminescence of Trivalent Lanthanide Impurities and Local Structure in  
539 CeO<sub>2</sub>-ZrO<sub>2</sub> Mixed Oxides. *M. Chem. Mater.* **2004**, *16*, 1938-1944.
- 540 (41) Sullivan, J.A.; Dulgheru, P.; Atribak, I.; Bueno-López, A.; García-García, A. Attempts at an in  
541 Situ Raman Study of Ceria/Zirconia Catalysts in PM Combustion. *Appl. Catal. B: Environ.* **2011**,  
542 *108-109*, 134-139.
- 543 (42) Nolas, S.; Tsoukala, V.G.; Gayen, S.K. Electronic-Raman-Scattering Study of the Low-Lying  
544 Energy Levels of Trivalent Cerium-Doped Yttria. *Phys. Rev. B* **1994**, *50*, 150-158.
- 545 (43) Füglein, E.; Hock, R.; Lerch, M. Crystal Structure and High Temperature Behavior of Zr<sub>2</sub>ON<sub>2</sub>.  
546 *Z. Anorg. Allg. Chem.* **1997**, *623*, 304.
- 547 (44) Yang, M.; Rodgers, J.A.; Middler, L.C.; Oró-Solé, J.; Jorge, A.B.; Fuertes, A.; Atfield, J.P.  
548 Direct Solid-State Synthesis at High Pressures of New Mixed-Metal Oxynitrides: RZrO<sub>2</sub>N (R = Pr,  
549 Nd, and Sm). *Inorg. Chem.* **2009**, *48*, 11498-11500.
- 550 (45) Nelson, A.E.; Schulz, K.H.; Surface Chemistry and Microstructural Analysis of Ce<sub>x</sub>Zr<sub>1-x</sub>O<sub>2-y</sub>  
551 Model Catalyst Surfaces *Appl. Surf. Sci.* **2003**, *210*, 206-221.
- 552 (46) Signore, M.A.; Rizzo, A.; Mirengi, L.; Tangliente, M.A.; Cappello, A.; Characterization of  
553 zirconium oxynitride films obtained by radio frequency magnetron reactive sputtering *Thin Solid*  
554 *Films* **2007**, *515*, 6798-6804.
- 555 (47) Roman, D.; Bernardi, J.; de Amorim, C.; de Souza, F.; Spinelli, A.; Giacomelli, C.; Figuero, C.;  
556 Baumvol, I.; Basso, R. Effect of Deposition Temperature on Microstructure and Corrosion Resistance  
557 of ZrN Thin Films Deposited by DC Reactive Magnetron Sputtering. *Mater. Chem. Phys.* **2011**, *130*,  
558 147-153.

- 559 (48) Qiu, L.; Liu, F.; Zhao, L.; Ma, Y.; Yao, J. Comparative XPS Study of Surface Reduction for  
560 Nanocrystalline and Microcrystalline Ceria Powder. *Appl. Surface Sci.* **2006**, *252*, 4931-4935.
- 561 (49) Chakraverty, S.; Mitra, S.; Mandal, K.; Nambissan, P.M.G.; Chattopadhyay, S. Positron  
562 Annihilation Studies of some Anomalous Features of NiFe<sub>2</sub>O<sub>4</sub> Nanocrystals Grown in SiO<sub>2</sub>. *Phys.*  
563 *Rev. B* **2005**, *71*, 024115.
- 564 (50) Dutta, S.; Chattopadhyay, S.; Jana, D.; Banerjee, A.; Manik, S.; Pradhan, S.K.; Sutradhar, M.;  
565 Sarkar, A. Annealing Effect on Nano-ZnO Powder Studied from Positron Lifetime and Optical  
566 Absorption Spectroscopy. *J. Appl. Physics* **2006**, *100*, 114328.
- 567 (51) Sanyal, D.; Banerjee, D.; De, U. (Bi<sub>0.92</sub>Pb<sub>0.17</sub>)<sub>2</sub>Sr<sub>1.91</sub>Ca<sub>2.03</sub>Cu<sub>3.06</sub>O<sub>10+δ</sub> Superconductors from 30  
568 to 300 K by Positron-Lifetime Measurements. *Phys. Rev. B* **1998**, *58*, 15226.
- 569 (52) Liu, X.; Zhou, K.; Wang, L.; Wang, B.; Li, Y. Oxygen Vacancy Clusters Promoting Reducibility  
570 and Activity of Ceria Nanorods. *J. Am. Chem. Soc.* **2009**, *131*, 3140–3141.
- 571 (53) Prochazka, I.; Cizek, J.; Melikhova, O.; Konstantinova, E.T.; Danilenko, I.A.; Yashehisyn, I.  
572 A.; Positron Annihilation Study of Zirconia Nanopowders and Nanoceramics Stabilized by Magnesia  
573 and Ceria. *J. Am. Ceram. Soc.* **2014**, *97*, 982-989.
- 574 (54) Kong, M.; Li, Y.; Chen, X.; Tian, T.; Fang, P.; Zheng, F.; Zhao, X. Tuning the Relative  
575 Concentration Ratio of Bulk Defects to Surface Defects in TiO<sub>2</sub> Nanocrystals Leads to High  
576 Photocatalytic Efficiency. *J. Am. Chem. Soc.* **2011**, *133*, 16414-16417.
- 577 (55) Zhao, Z.; Uddi, M.; Tsvetkov, N.; Yildiz, B.; Ghoniem A.F. Redox Kinetics Study of Fuel  
578 Reduced Ceria for Chemical-Looping Water Splitting. *J Phys. Chem. C* **2016**, *120*, 16271-16269.
- 579 (56) Lerch, M. Nitridation of Zirconia. *J Am. Ceram. Soc.* **1996**, *79*, 2641-2644.
- 580 (57) Chen, B.; Ma, Y.; Ding, L.; Xu, L.; Wu, Z.; Yuan, Q.; Huang, W. Reactivity of Hydroxyls and  
581 Water on a CeO<sub>2</sub>(111) Thin Film Surface: The Role of Oxygen Vacancy. *J. Phys. Chem. C.* **2013**,  
582 *117*, 5800-5810.
- 583 (58) Wu, X.P.; Gong, X.-Q. Clustering of Oxygen Vacancies at CeO<sub>2</sub>(111): Critical Role of  
584 Hydroxyls. *Phys. Rev. Lett.* **2016**, *116*, 086102, 1-6.
- 585 (59) Wu, X.P.; Gong, X.-Q.; Lu, G. Role of Oxygen Vacancies in the Surface Evolution of H<sub>2</sub> at  
586 CeO<sub>2</sub>(111): a Charge Modification Effect. *Phys. Chem. Chem. Phys.* **2015**, *17*, 3544-3549.
- 587 (60) Feng, A.; Galaby, F.E.; Ye, X.; Shen, Z.-X. Chueh, W.C. Fast Vacancy-Mediated Oxygen Ion  
588 Incorporation Across the Ceria-Gas Electrochemical Interface. *Nature Comm.* **2014**, *5*, 1-8.
- 589 (61) Atfield, J.P. Principles and Applications of Anion Order in Solid Oxynitrides. *Cryst. Growth*  
590 *Des.* **2013**, *13*, 4623-4629.

591

592

593  
594  
595  
596  
597  
598  
599  
600  
601  
602  
603  
604  
605  
606  
607  
608  
609  
610  
611  
612  
613  
614  
615  
616  
617  
618  
619  
620

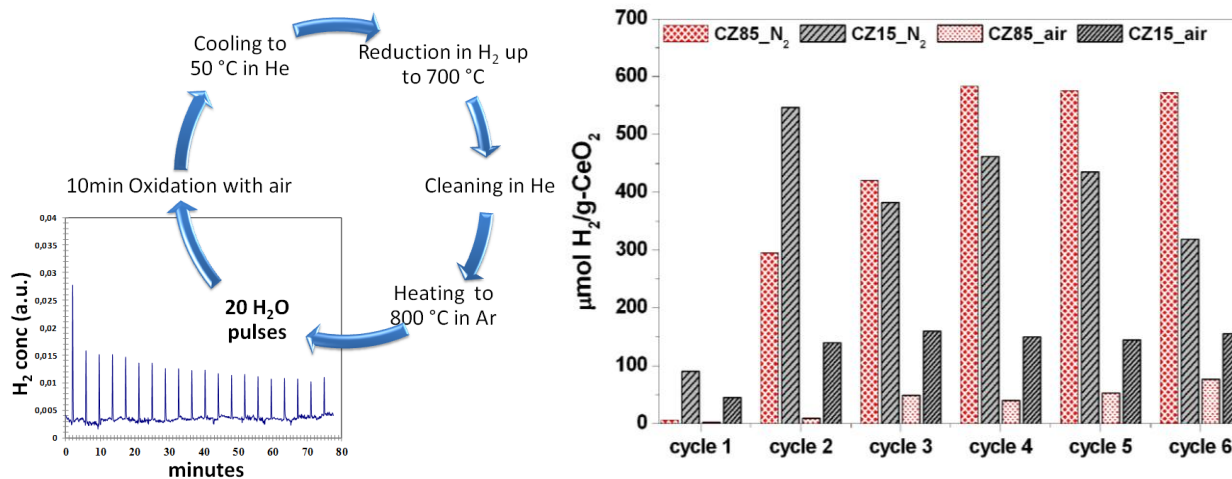


**Figure 1:** Comparison between water splitting reactivity of CZ85 and of CZ15<sup>27</sup> pretreated in N<sub>2</sub> or Air at 1300 °C/4h. On the right, schematic of one typical cycle.

621

622

623

624

625

626

627

628

629

630

631

632

633

634

635

636

637

638

639

640

641

642

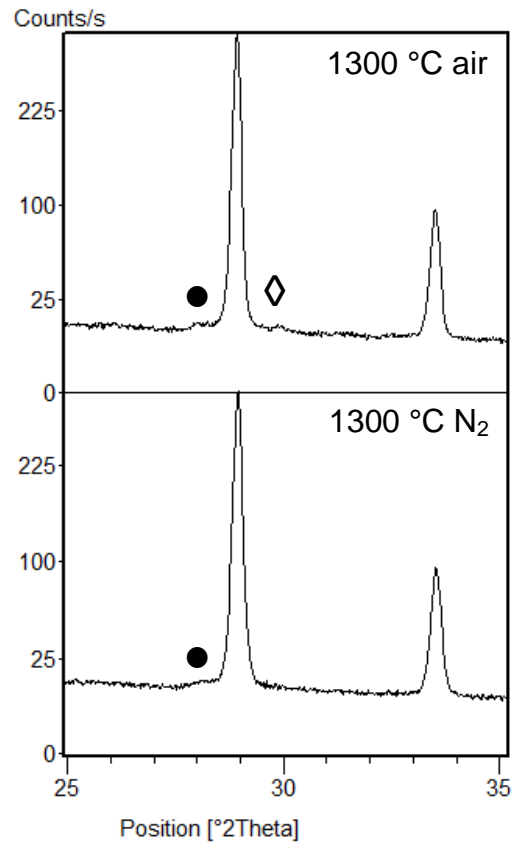
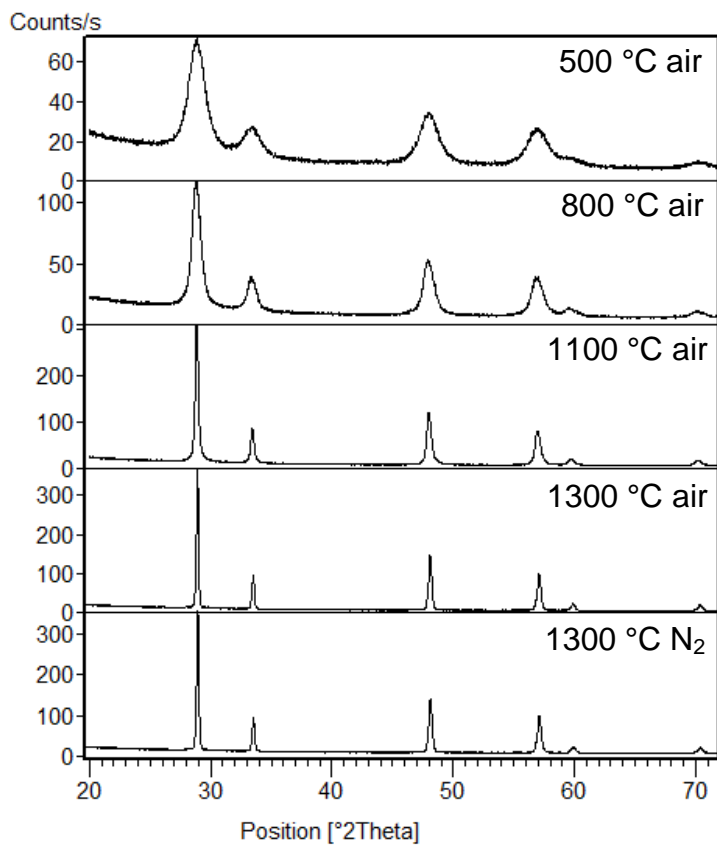
643

644

645

646

647



648 **Figure 2:** X-ray profiles of  $\text{Ce}_{0.85}\text{Zr}_{0.15}\text{O}_2$  calcined at different temperatures in air and at 1300 °C in  
649  $\text{N}_2$  flow. To the right: details of samples treated at 1300 °C/4h. Symbols indicate the segregated  
650 crystal phases : ●  $\text{Ce}_{0.05}\text{Zr}_{0.95}\text{O}_2$  (PDF 88-2392); ◇  $\text{Ce}_{0.18}\text{Zr}_{0.82}\text{O}_2$  (PDF 80-0785).

651

652

653

654

655

656

657

658

659

660

661

662

663

664

665

666

667

668

669

670

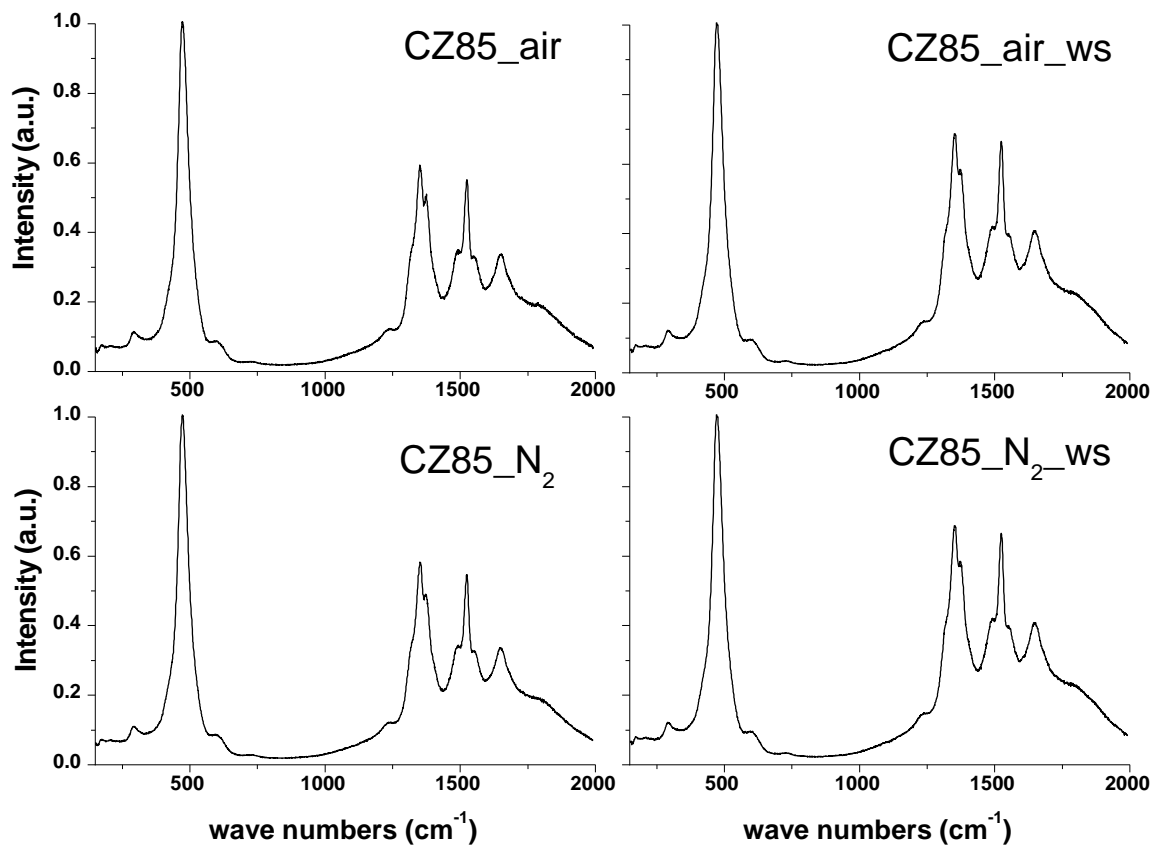
671

672

673

674

675



676

677

678 **Figure 3:** Raman spectra of CZ85 treated in air before(CZ85\_air) and after six water splitting  
679 cycles (CZ85\_air\_ws) or in N<sub>2</sub> before (CZ85\_N<sub>2</sub>) and after six water splitting cycles  
680 (CZ85\_N<sub>2</sub>\_ws). Spectra collected using an excitation radiation at 785 nm.

681

682

683

684

685

686

687

688

689

690

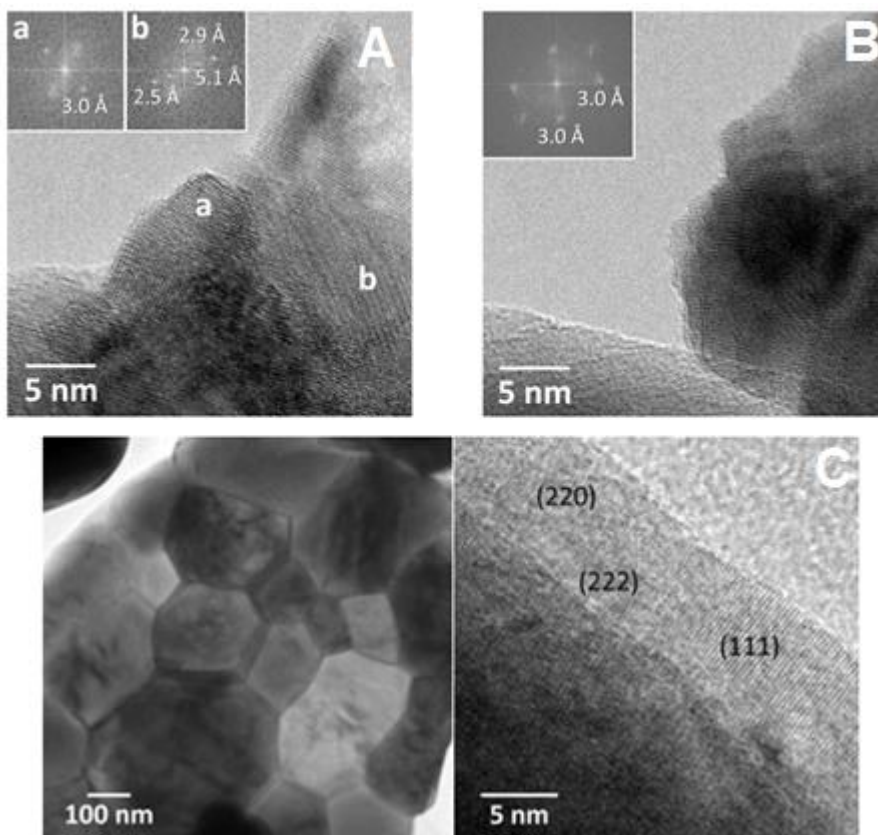
691

692

693

694

695



696

697

698

699

700

701

702

703 **Figure 4:** HRTEM of Ce<sub>0.85</sub>Zr<sub>0.15</sub>O<sub>2</sub> (CZ85) treated at 1300 °C/4h: A) in N<sub>2</sub>; B) in air; C) images of  
704 the sample treated in N<sub>2</sub> after water splitting test.

705

706

707

708

709

710

711

712

713

714

715

716

717

718

719

720

721

722

723

724

725

726

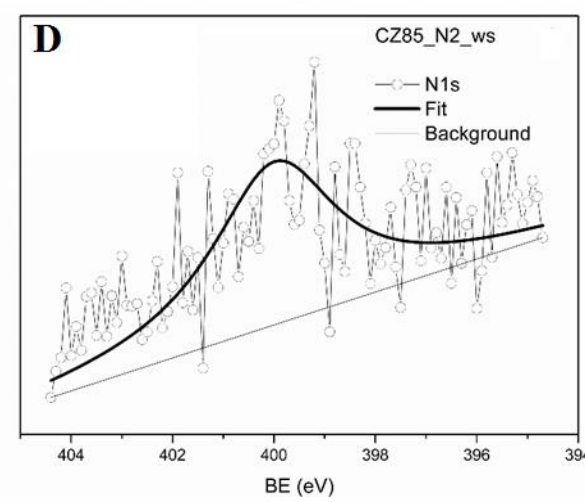
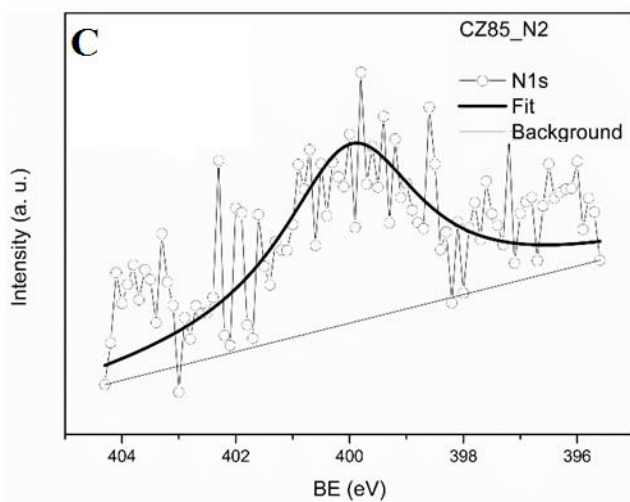
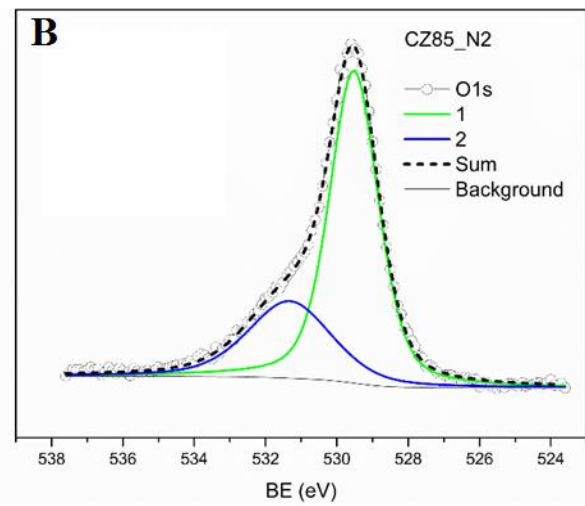
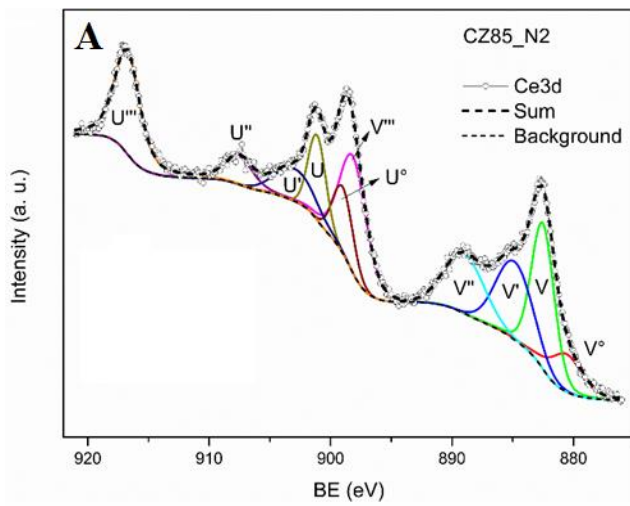
727

728

729

730

731



732

733

734

735

736 **Figure 5:** XPS spectra of CZ85 treated in N<sub>2</sub> 1300 °C/4h. Figures show Ce3d, O1 and N1s regions  
737 and related fitting components.

738

739

740

741

742

743

744

745

746

747

748

749

750

751

752

753

754

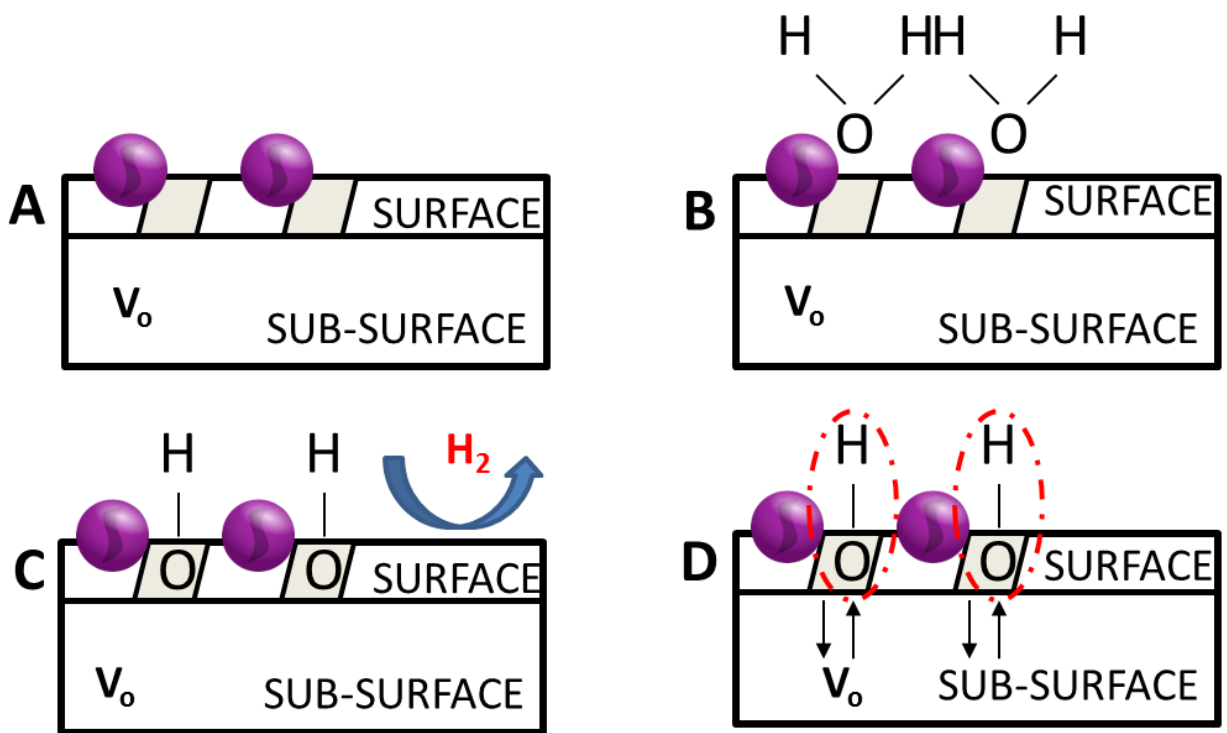
755

756

757

758

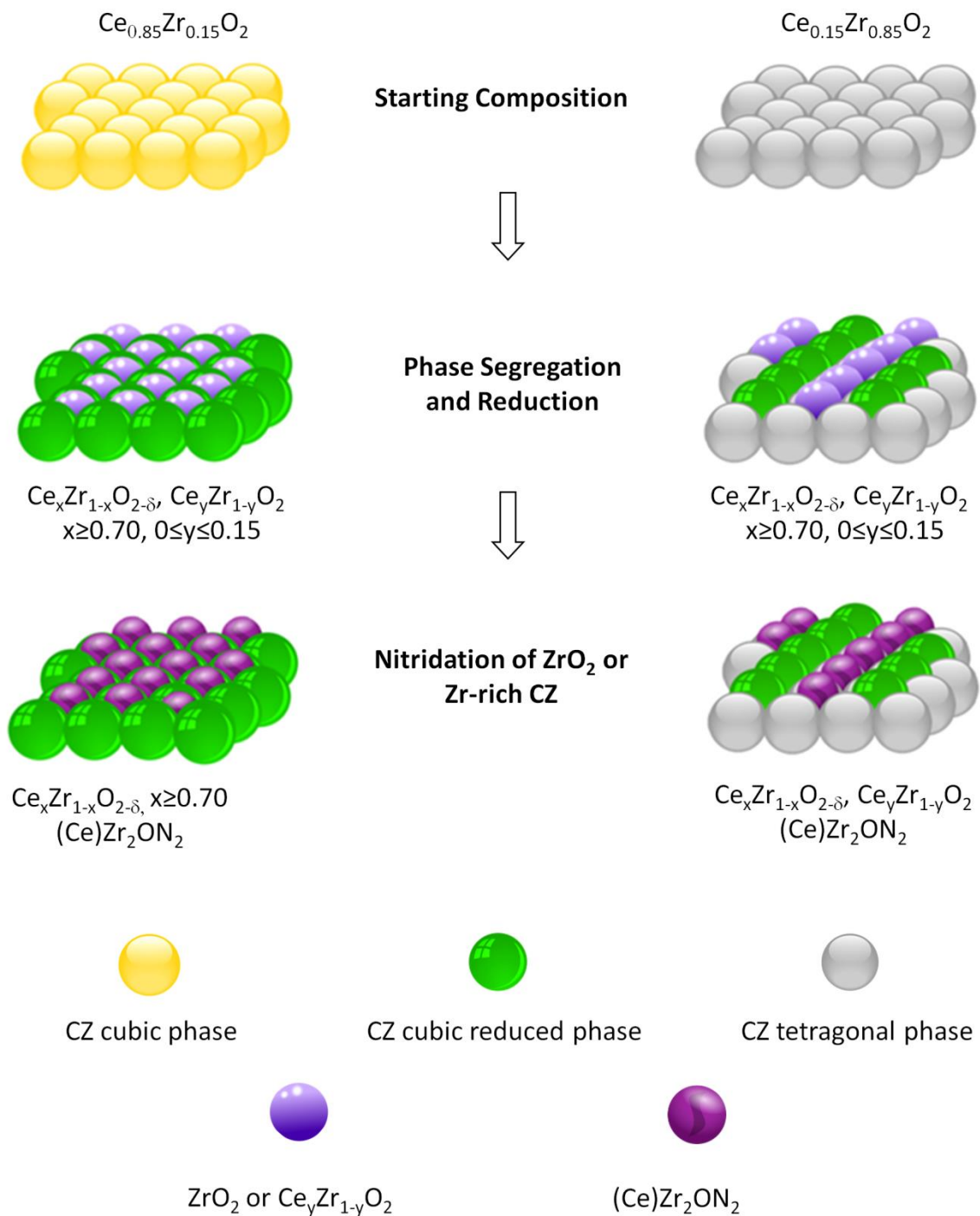
759



Vacancy clusters   
  $V_o$  Oxygen vacancies   
  (Ce)Zr<sub>2</sub>ON<sub>2</sub>

760 **Figure 6:** Surface activation mechanism of CZ80 doped with a zirconium oxynitride phase: A)  
 761 (Ce)Zr<sub>2</sub>ON<sub>2</sub> contributes to form and stabilize large vacancy clusters (VC) on the surface; B-C) water  
 762 is adsorbed on VCs forming surface hydroxyl groups (OHs), D) hydroxylated clusters favour the  
 763 incorporation of OHs into the subsurface layers and oxygen vacancies migration from the bulk, such  
 764 configuration boosts the production of H<sub>2</sub> from the second redox cycle.

765



766

767

768 **Figure 7:** Schematic of segregation processes at 1300 °C in N<sub>2</sub> atmosphere of CZ85 and CZ15.

769

770

771

772 **TABLE OF CONTENTS (TOC) IMAGE**

773

774

775

776

777

